Unveiling precipitation behavior in Mg-Y based alloys

Qingchun Zhu [a], Yangxin Li [a,*], Zhigang Ding [b], Jian Wang [c], Yuxuan Liu [a], Huan Zhang [a], Tian Xie [a], Mingxu Wang [a], Hong Zhu [d], Tao Ying [a], Wei Liu [b], Xiaoqin Zeng [a,*]

[a] National Engineering Research Center of Light Alloy Net Forming and State Key Laboratory of Metal Matrix Composite, Shanghai Jiao Tong University, 200240 Shanghai, PR China
[b] Nano and Heterogeneous Materials Center, School of Materials Science and Engineering, Nanjing University of Science and Technology, Nanjing 210094, PR China
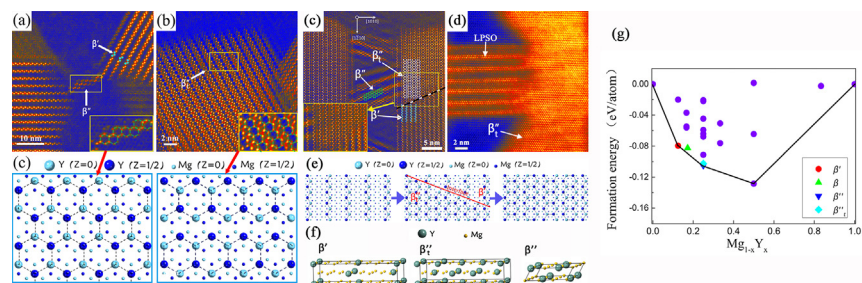[c] Mechanical and Materials Engineering, University of Nebraska-Lincoln, Lincoln, NE 68588, USA
[d] University of Michigan-Shanghai Jiao Tong University Joint Institute, Shanghai Jiao Tong University, 200240 Shanghai, PR China

HIGHLIGHTS

- A new precipitation sequence, SSSS → clusters/G.P. Zones → β' (Mg_7Y) → β''/β_t'' (Mg_3Y), is observed in Mg-Y based alloys.
- The β_t'' phase, which has a Mg_3Y composition and a $cbco$ structure, is in-situ transformed from the β' phase.
- The β_t'' phase is stable after long-time exposure at elevated temperature.

GRAPHICAL ABSTRACT

ARTICLE INFO

ABSTRACT

Mg-Y based alloys exhibit a promising combination of strength and deformability through tuning precipitation and solute strengthening mechanisms and tailoring the activity of non-basal dislocations. Understanding the precipitation sequence of Mg-Y based alloys and its dependence on Yttrium concentration in the matrix will provide a guideline for fine tuning structure, morphology and distribution of precipitates in Mg-Y based alloys. In this paper, we explore the precipitation behaviors of Mg-11Y (wt%) and Mg-11Y-1Al (wt%) alloys using aberration-corrected scanning transmission electron microscopy, and rationalize the experimental observations based on first-principles density functional theory calculations. The precipitation sequence during ageing at 225 °C is identified to be SSSS → clusters/G.P. Zones → β' (Mg_7Y) → β''/β_t'' (Mg_3Y). A novel β_t'' phase forms through in-situ transformation from the β' phase, which shares the same Mg_3Y composition with $D0_{19}$-β'' phase and exhibits the same $cbco$-structure as β' phase in Mg-Y based alloys.

1. Introduction

Precipitation strengthening mechanisms are widely applied for development of high strength Magnesium (Mg) alloys [1]. Alloying with other elements, such as zinc, aluminum or/and rare earth (RE) elements, has been demonstrated to significantly manipulate mechanical properties of Mg alloys [1–4]. Particularly, RE addition can tailor deformation modes [5] and tune precipitates with different phases [3,6,7]. As the lightest and cheapest heavy RE elements, Yttrium (Y) can

strengthen Mg alloys via precipitation hardening [8] and improve deformability of Mg alloys via enhancing activity of non-basal dislocations [9]. To date, Mg-Y based alloys containing long-period stacking ordered (LPSO) phase have drawn considerable attentions because they can exhibit the highest yield strength (>600 MPa) among other Mg alloys [10]. Via high-resolution transmission electron microscopy (HRTEM), such a unique LPSO phase has been confirmed to exhibit different polytypes, such as 14H [11] and 18R [11], which refer to different stacking sequences along the (0002) basal plane.

Mechanical properties of Mg-Y based alloys are highly correlated to distribution, morphology and phase structure of precipitates [1]. Understanding precipitation behavior and phase equilibria of Mg-Y based

* Corresponding authors.
E-mail addresses: astatium@sjtu.edu.cn (Y. Li), xqzeng@sjtu.edu.cn (X. Zeng).

alloys at given temperatures will enable optimizing thermal treatment processing. For Mg-Y based alloys, the β' phase (Mg_7Y) with a *c*-axis base-centered orthorhombic structure (*cbco*, $a = 0.64$ nm, $b = 2.24$ nm, $c = 0.52$ nm) is commonly accepted as a key strengthening phase because it forms on prismatic planes during ageing at lower temperatures (≤ 250 °C) [1]. By using high-angle annular dark-field scanning transmission electron microscopy (HAADF-STEM), Nishijima et al. [12] identified that the Y atoms were ordered at certain zigzag sites with three distinct variants. Unlike the β' phase, the β phase ($Mg_{24}Y_5$, *bcc*, $a = 1.13$ nm) was only observed during ageing at $T \geq 300$ °C [13–15]. The precipitation sequence of Mg-Y binary alloys was proposed to be SSSS $\rightarrow \beta' \rightarrow \beta$ [16], where SSSS is the abbreviation of "supersaturated solid solution". However, no direct evidence supports the $\beta' \rightarrow \beta$ transformation under isothermal ageing [14]. In addition, first-principles density functional theory (DFT) calculations indicate that the β' and β phases are energetically competitive [16].

Apart from the β' and β phases, G.P. zones with short-range ordering of RE atoms in the form of zig-zag lines have been observed during the early-stage decomposition of SSSS in several binary Mg-RE alloys [17–20], but rarely characterized in Mg-Y alloys [21]. Although the β'' phase (Mg_3RE) with a $D0_{19}$ structure ($a = 0.64$ nm, $c = 0.52$ nm) has been reported in some binary Mg-RE alloys [22,23], it is clearly observed with only 2–3 unit cells in size in a ternary Mg-Gd-Y alloy [24]. Since the β'' phase was not characterized in many binary Mg-RE alloys, Nie et al. [21] suggested that the β'' phase could be an unstable phase. Hence, the open questions are whether the G.P. zones and β'' phase form in Mg-Y alloys and how they are involved in precipitation process.

Precipitation is the product of "excess" alloying. Via controlling Y concentration within the matrix of Mg-Y based alloys, the density and uniformity of dispersing precipitates can be adjusted during isothermal ageing. To explore precipitation behavior of Mg-Y based alloys, we characterized precipitates in nominal Mg-11Y and Mg-11Y-1Al (wt %) alloys using atomic-resolution HAADF-STEM, and rationalized our findings based on DFT calculations. The Mg-Y-Al system is chosen for this study because the addition of Al can refine the grain size dramatically and introduce the 18R-LPSO phase with the excellent thermal stability [10,25–27], which can tune the distribution of precipitates and inhibit the coarsening of precipitates during long-time exposure. In addition, the influence of LPSO phase on precipitation behavior in Mg-Y based alloy is still unclear. Our work reveals an undiscovered precipitation behavior that a novel β_t'' phase is identified to exhibit an in-situ transformation from β' phase. The precipitation sequence of Mg-Y based alloys is thus identified as SSSS $\rightarrow$ clusters/G.P. Zones $\rightarrow \beta'$ (Mg_7Y) $\rightarrow \beta''/\beta_t''$ (Mg_3Y). Our finding provides a guideline for fine tuning structure, morphology and distribution of precipitates in Mg-Y based alloys.

2. Methods

2.1. Specimen preparation

Mg-11Y (wt%) melts were firstly prepared in a BN-coated steel crucible at 750 °C in a protective atmosphere of mixed CO_2 and SF_6 in dry air by melting pure Mg ingot (99.5 wt%) and Mg-25Y (wt%) master alloy. Then, 1.0 wt% pure Al ingot (99.9 wt%) was added into one of the melts and isothermally held for 30 min before casting into a steel model preheated at 200 °C. Thus, two alloys were made, with nominal compositions of Mg-11Y and Mg-11Y-1Al, respectively. Chemical compositions of these two alloys measured by Inductive Coupled Plasma Emission Spectrometer are listed in Table 1. In order to obtained microstructure with different LPSO amount and distribution, the casting Mg-11Y-1Al alloy was homogenized at 550 °C for 16 h and 520 °C for 8 h, respectively, whereas the Mg-11Y alloy was homogenized at 525 °C for 16 h which the primary phases could be dissolved into the matrix as much as possible followed by water quenching at ambient

Table 1
Chemical compositions of the studied Mg-Y and Mg-Y-Al alloys.

Alloys (wt%)	Y	Al	Mg
Mg-11Y	11.21	0	Bal.
Mg-11Y-1Al	10.83	1.09	Bal.

temperature. Then, all the homogenized alloys were aged at 225 °C for different time intervals ranging from 1 min to 100 days. Vickers hardness tests were carried out with a 5 kg load holding for 15 s. For each sample, the hardness was measured at eight different positions and an average value was calculated with an error-bar. Metallographic samples were cut from the ingots and examined by optical microscope (OM) using a Zeiss Axioscope 5 machine. Energy dispersive X-ray Spectroscopy (EDS) analyses were conducted in a Phenom ProX scanning electron microscope (SEM). The volume fractions of LPSO phase in different Mg-Y-Al alloys were statistically estimated from several OM images.

2.2. Transmission electron microscopy

TEM specimens were cut into foils with a height of ~0.8 mm and thinned to a thickness of ~150 μm. Discs with 3 mm in diameter were punched from the foils and further thinned to ~70 μm, followed by twin-jet electro-polished in an ethanol solution with 4 pct perchloric acid. Afterwards, the specimens were perforated in a Gatan 695 ion-milling system with 1 KeV for 30 mins. HAADF-STEM images were obtained using a JEOL-ARM200 microscope operating at 200 kV. All the HAADF-STEM images were processed by masking diffraction spots in the fast Fourier transform and then back-transformed using Gatan Digital Microscopy. Since the brightness of individual atomic columns in HAADF-STEM images is proportional to the square of the averaged atomic number, each bright spot represents a Y-rich column herein.

Simulated HAADF-STEM images were obtained by JEMS software based on the conventional multi-slice method [24], of which the conditions are listed as follows: high voltage $= 200$ kV, Cs $= 0$ mm, convergence angle $= 12.5$ mrad, probe sampling $= 0.05$ $\dot{A}$/px, probe semi-angle $= 12.5$ mrad, inner aperture $= 90$ mrad and outer aperture $= 170$ mrad.

2.3. DFT simulation

All DFT calculations are performed using the Vienna Ab initio Simulation Package (VASP) [28–30]. We used the projector augmented wave (PAW) formalism [31–33]. For all calculations, the G-centered k-point meshes with about 5000 k-points per reciprocal atom and a plane-wave cutoff energy of 360 eV were adopted. The energy tolerance for the electronic relaxations was set to be 10^{-6} eV per atom, and the Hellmann-Feynman force tolerance for the ion relaxations was set to be 0.01 eV/Å.

The convex hull of formation energy was calculated using the Alloy Theoretic Automated Toolkit (ATAT) [34–36], where the formation energy of a binary compound A_mB_n, $\Delta H_f (A_mB_n)$, is given by the difference between the energy of A_mB_n and the composition-weighted average energies of the pure constituents in their ground state crystal structures:

$$\Delta H_f(A_mB_nC_l) = E(A_mB_nC_l) - \frac{m}{m+n+l}E(A) - \frac{n}{m+n+l}E(B) - \frac{l}{m+n+l}E(C) \tag{1}$$

where $E(A_mB_nC_l)$, $E(A)$, $E(B)$ and $E(C)$ are the DFT-calculated total energies of the compound $A_mB_nC_l$, constituents pure A, B and C in their equilibrium crystal structures, respectively. In this paper, A, B and C represent Mg, Y and Al, respectively.
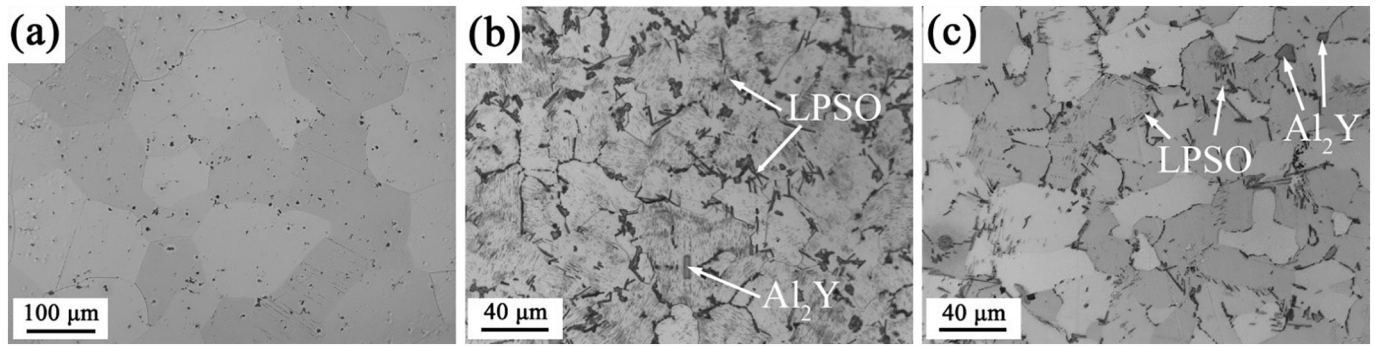
Fig. 1. Optical micrographs of (a) Mg-11Y alloy after 525 °C-16 h homogenization; (b) Mg-11Y-1Al alloy after 520 °C-8 h homogenization; (c) Mg-11Y-1Al alloy after 550 °C-16 h homogenization.
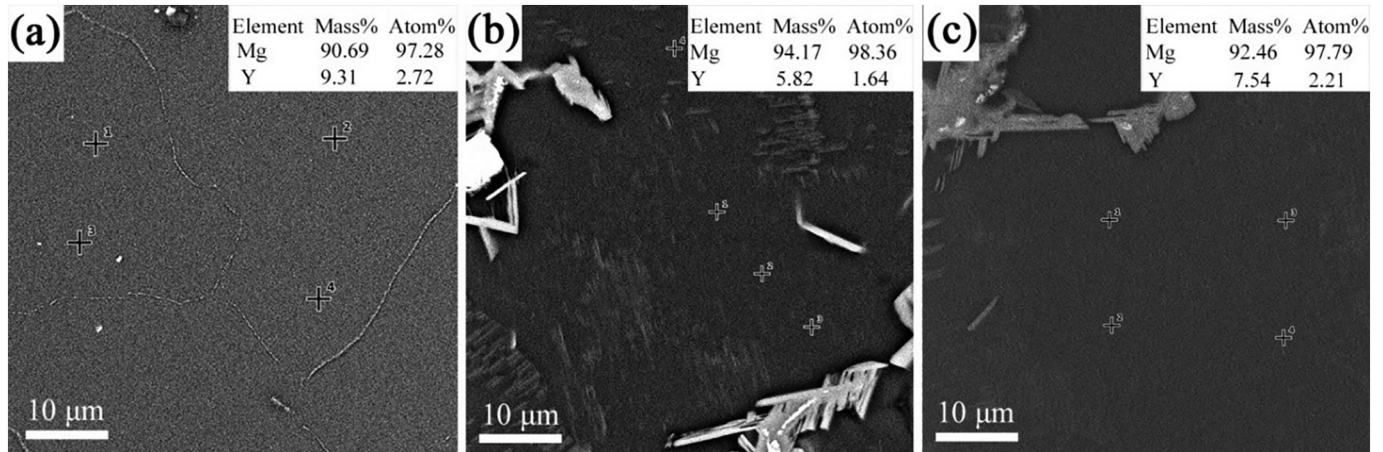

Fig. 2. EDS results of Y concentrations within the matrix of (a) 525 °C-homogenized Mg-11Y alloy; (b) 520 °C-homogenized Mg-11Y-1Al alloy; (c) 550 °C-homogenized Mg-11Y-1Al alloy, respectively.

3. Results

3.1. Precipitates in Mg-Y based alloys

The metallographic results of the Mg-Y alloy and Mg-Y-Al alloy after homogenized treatment are shown in Figs. 1a, b and c. After homogenization at 525 °C for 16 h, the average grain size of ~200 μm is obtained and no obviously precipitate exist in Mg-11Y alloy after solution treatment, as shown in Fig. 1a. In contrast, the homogenized Mg-11Y-1Al alloys in Fig. 1b (520 °C for 8 h) and Fig. 1c (550 °C for 16 h), though share a smaller average grain size of ~40 μm, cannot completely dissolve the LPSO and Al$_2$Y phases into the matrix. In addition, the
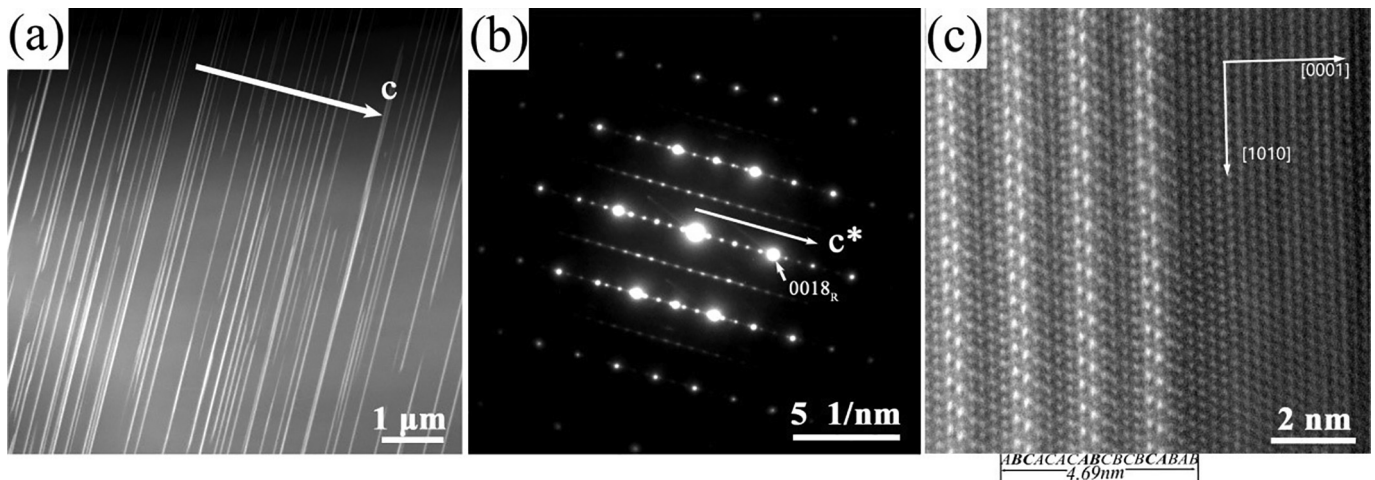

Fig. 3. HAADF-STEM image (a) of fine 18R-LPSO lamellas in the matrix of the 520 °C-homogenized Mg-11Y-1Al alloy, with the corresponding selected area electron diffraction (SAED) pattern shown in (b) and (c) shows the stacking sequence of 18R polytype.
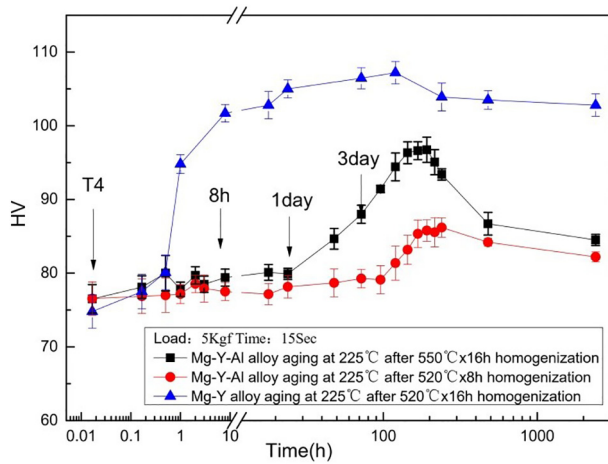
Fig. 4. Ageing curves of the Mg-11Y and Mg-11Y-1Al alloys.

volume fractions of LPSO phase in the 520 °C-homogenized and 550 °C-homogenized Mg-11Y-1Al alloys are 17% and 6.5%, respectively.

The alloying elements within of the matrix were determined by EDS analyses and the results are shown in Fig. 2, where the average Y concentrations within the matrix were obtained based on each four individual tests, respectively. Compared with the Y concentration in binary Mg-11Y alloy (9.31 wt%), the Y concentration in the matrix is decreased in ternary Mg-11Y-Al alloy, but a higher Y concentration is obtained within the matrix of the 550 °C-homogenized Mg-11Y-1Al alloy (7.54 wt%) than that of the 520 °C-homogenized Mg-11Y-1Al alloy (5.82 wt%), which can be manipulated via controlling the volume

fractions of LPSO phase during heat treatment. The LPSO phase in the Mg-11Y-1Al was identified to exhibit an 18R polytype, with a stacking sequence of *ABC*ACAC*AB*CBCB*CA*BAB shown in Fig. 3.

Emphasis of this study was laid on the precipitation behavior of the Mg-Y based alloys during the ageing process. The ageing curves were determined by measuring the HV after different ageing times. Fig. 4 presents the ageing curves of the Mg-11Y alloy at 225 °C after 525 °C-homogenization, and Mg-11Y-1Al alloys at 225 °C after 520 °C-homogenization and 550 °C-homogenization, respectively. The HV of Mg-11Y is higher than that of the Mg-11Y-1Al alloys after 1 h ageing, indicating that the precipitation hardening is more pronounced in the Mg-11Y alloy. Since the precipitation hardening of the 520 °C-homogenized Mg-11Y-1Al alloy is insignificant, it is necessary to adjust the homogenization parameters to see whether a notable hardening effect can be achieved during ageing. It is obvious that the 550 °C-homogenized Mg-11Y-1Al alloy performs a much better precipitation hardening than that of the 520 °C-homogenized Mg-11Y-1Al alloy.

To uncover the cause of different age hardening behaviors of the alloys, the precipitates at different ageing stages were carefully examined by TEM. Figs. 5a and b show the coarse precipitates in the aged Mg-11Y alloy after long-time exposure at 225 °C for 2400 h. With 1 wt. pct Al addition, uniform 18R-LPSO lamellas were introduced in the casting Mg-11Y-1Al alloy after homogenized at 520 °C for 8 h in Fig. 5c, which could provide strong inhibitors for precipitate coarsening during long-time ageing.

Although the formation of these LPSO lamellas significantly lower the Y concentration within the matrix, reducing the density of precipitates (Figs. 5c and d) and weakening the age-hardening effect (Fig. 4), they can strongly inhibit the precipitate coarsening along [0001] direction (Fig. 5c) and enable a much finer distribution of precipitates in the Mg-11Y-1Al alloy (Fig. 5d) after ageing 225 °C for 2400 h.
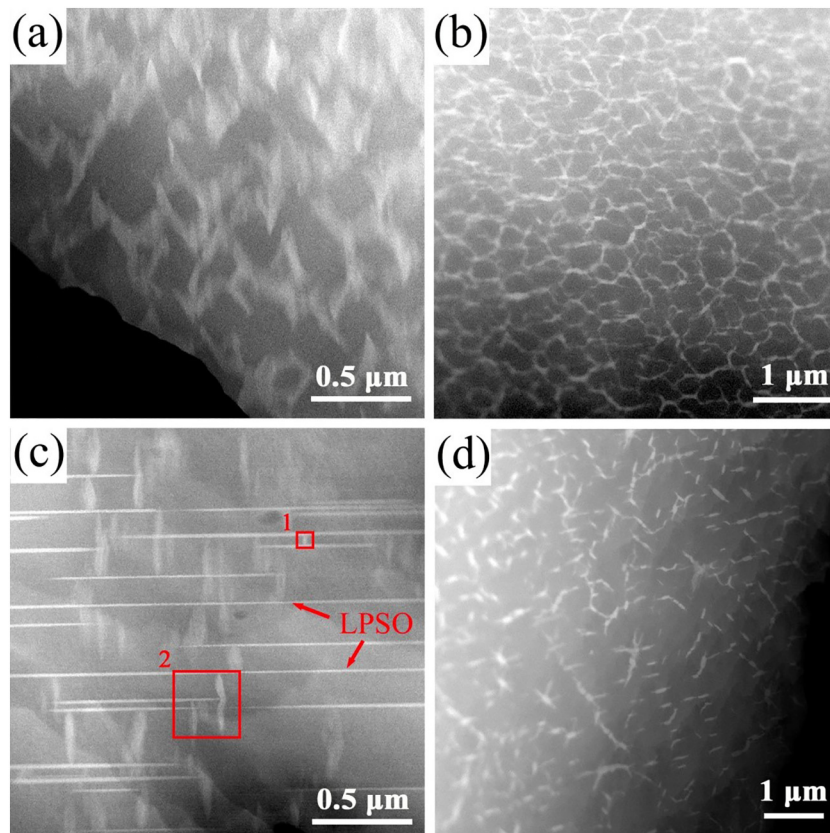

Fig. 5. HAADF-STEM images showing the precipitate features of (a-b) 525 °C homogenized Mg-11Y and (c-d) 520 °C homogenized Mg-11Y-1Al alloys after ageing at 225 °C for 2400 h. (a) and (c) are viewed along $[11\bar{2}0]_\alpha$, whilst (b) and (d) are viewed along $[0001]_\alpha$. The selected areas "1" and "2" are enlarged in Fig. 9d and e, respectively.
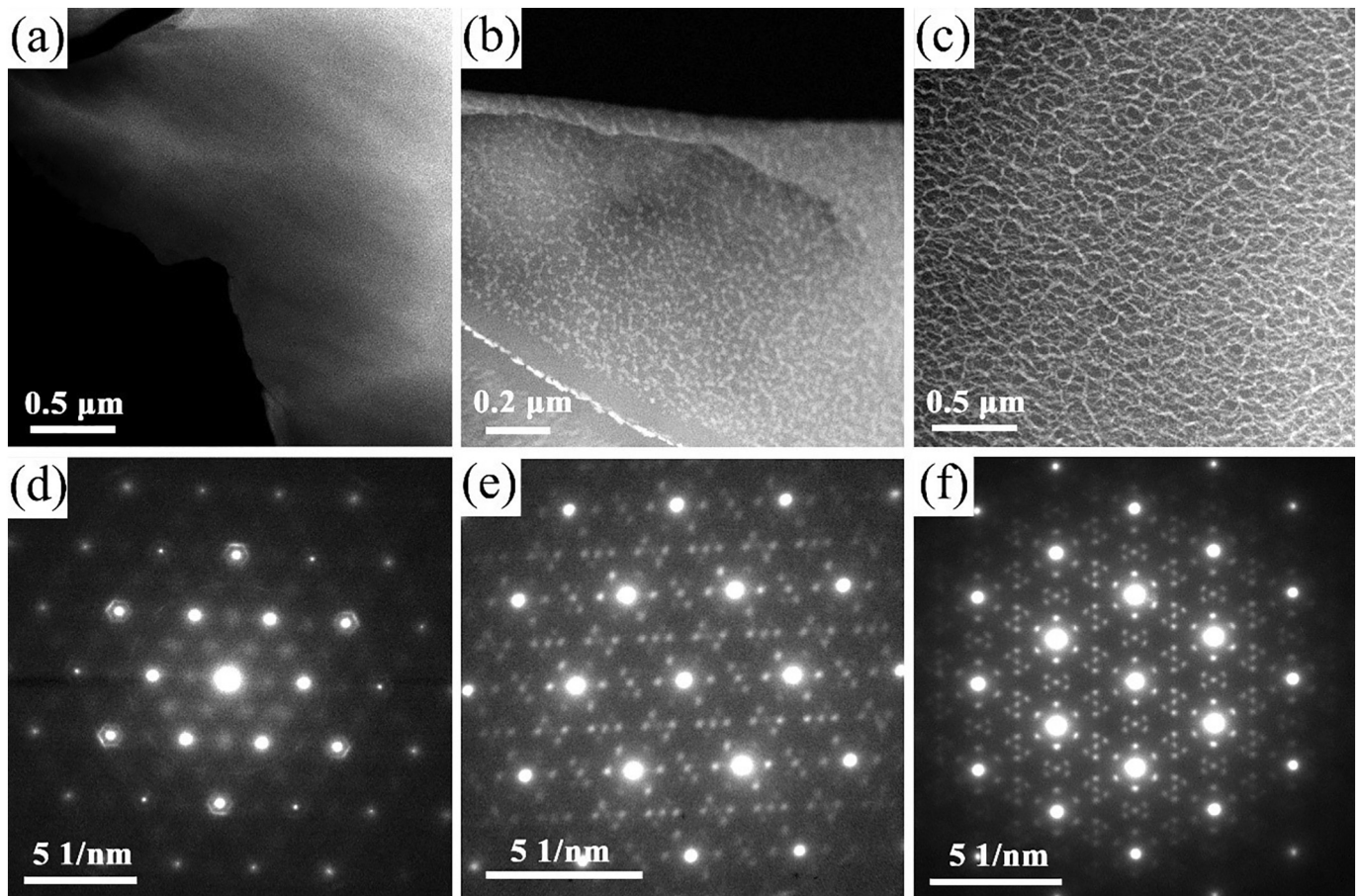
Fig. 6. HAADF-STEM images showing the distribution of precipitates in the Mg-11Y alloys aged at 225 °C for (a) 30 min, (b) 24 h and (c) 480 h, with the corresponding SAED patterns shown in (d-f), respectively. The incident beam is parallel to the $[0001]_\alpha$ zone axis.

When the casting Mg-11Y-1Al alloy was homogenized at 550 °C for 16 h, we obtained a lower volume fraction of LPSO phase and a higher Y concentration within the matrix, leading to a higher Vickers hardness in the Mg-11Y-1Al alloy after long-time exposure at 225 °C. Therefore, it is feasible to control the mechanical properties via manipulating the distribution of LPSO phases and Y concentration within the matrix in Mg-Y based alloys. More importantly, some new precipitation phenomena are observed in these Mg-Y based alloys. In order to explore precipitation behaviors in these Mg-Y based alloys, we systematically characterized phase structure and morphology of these precipitates and their evolution during ageing.

3.2. Precipitation behavior of binary Mg-11Y alloy

After ageing Mg-11Y alloy for 30 mins, Fig. 6a shows the low-magnification HAADF-STEM image, no apparent precipitates are observed. Fig. 6d shows the corresponding SAED pattern that indicates the formation of $D0_{19}$-β'' structures in the matrix. The enlarged HAADF-STEM image in Fig. 7a further reveals that the $D0_{19}$-β'' structures are presented as discretized clusters. When the ageing time was increased to 24 h, a high density of β' phase precipitates was obtained in the matrix, as shown in Fig. 6b. These precipitates form a fine network after ageing for 480 h, as shown in Fig. 6c. It is noticed that the SAED pattern in Fig. 6f show only the β' phase, but the atomic resolution HAADF-STEM image in Fig. 7d does suggest the appearance of β_t'' phase.

Fig. 7a shows a representative HAADF-STEM image of the Mg-11Y alloy aged for 0.5 h after homogenizing at 525 °C for 16 h, with the incident beam parallel to $[0001]_\alpha$ zone axis. At the very beginning stage of ageing, some isolated solute clusters with a few Y-rich columns were

randomly distributed in the matrix. It is worth mentioning that these clusters commonly comprise neighboring hexagons which correspond to two unit cells of an ordered $D0_{19}$-β'' structure, as further captured by the SAED pattern in Fig. 6d. Such a finding indicates that the β'' phase could be stable in the Mg-Y based alloys under certain circumstance. When the ageing time reached 2 h, the regular zig-zag shaped mono-layer G.P. zones were commonly found in the matrix, with an ordered arrangement of Y-rich columns along the $<11\bar{2}0>_\alpha$ direction, as shown in Fig. 7b. With increasing the ageing time to 24 h, G.P. zones were gradually evolved into the β' phase. It is notable that the β' phase at this peak-aged condition is made of three successive G.P. zones, with two adjacent G.P. zones in opposite directions, as shown in Fig. 7c. In addition, a strand of hexagons, which is usually interleaved between the zig-zag rows of two β' particles, is confirmed to be the $D0_{19}$-β'' phase. After ageing for 480 h, a novel phase (denoted as β_t'') was transformed from the β' phase, as shown in Fig. 7d. The β_t'' phase looks like the $D0_{19}$-β'' phase at the first glance. However, the arrangement of hexagons in β_t'' phase is indeed different from that in $D0_{19}$-β'' phase when viewing along $[0001]_\alpha$ zone axis (as illustrated in Fig. 7e), although the β_t'' phase exhibits the same Y concentration with the β'' phase (Mg_3Y).

In order to confirm the formation of such a novel β_t'' phase and determine its structure, we extended the ageing time to 2400 h and further characterized the structure in different viewing directions. Fig. 8a shows a representative morphology of precipitates viewing along $[0001]_\alpha$ zone axis after ageing at 225 °C for 2400 h, and the Fig. 8b is the corresponding enlargement in Fig. 8a. The contrast of Y atom columns is uniform and exhibits identical distribution with that in Fig. 8d, which confirms the formation of β_t'' phase. When the viewing
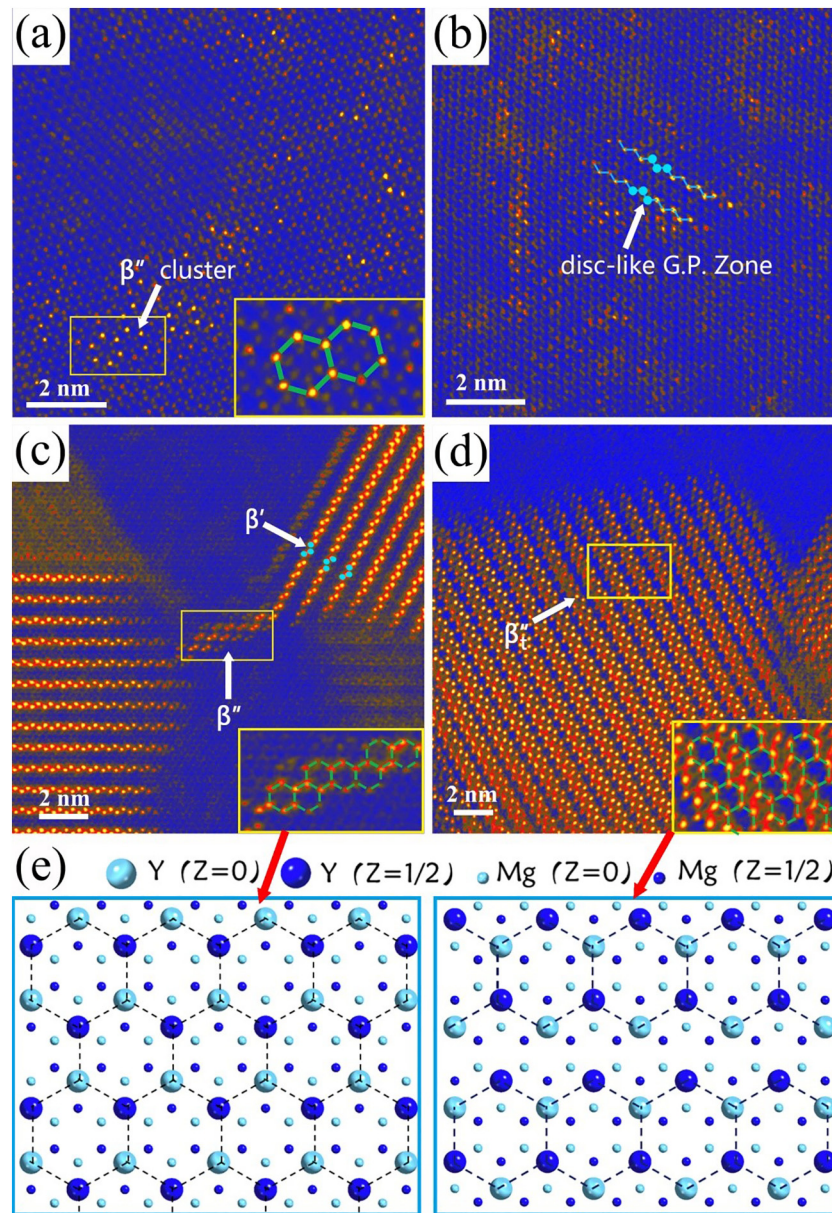
Fig. 7. HAADF-STEM images of the Mg-11Y alloys aged for: (a) 0.5 h; (b) 2 h; (c) 24 h; (d) 480 h; (e) schematic diagrams showing the different Y occupations of β'' and β_t'' precipitates, respectively. The viewing direction is parallel to $[0001]_\alpha$ in this figure.

direction is tilted to $\left[11\overline{2}0\right]_\alpha$ zone axis, the β_t'' phase usually exhibits a "wheat-kernel" shape, as shown in Fig. 8c. The enlargement area in Fig. 8d shows an unfrequent projection which provides more information to establish the crystal structure of β_t'' phase.

3.3. Precipitation behavior of Mg-11Y-1Al alloy

For the Mg-11Y-1Al alloy, we also observed the β' precipitates after ageing. However, the density of β' phase differs from that in the Mg-11Y alloy. With increasing the ageing time, the precipitate density of β' phase in the 520 °C-homogenized Mg-11Y-1Al alloy (Fig. 5c and d) was much lower than that of Mg-11Y alloy (Fig. 5a and b). Fig. 9a shows that most β' precipitates were connected by strands of β'' precipitates emanating from their corners when the peak-aged condition was achieved after peak-ageing for 240 h, while the β_t'' phase was rarely found at this stage. When the ageing time was prolonged to 2400 h, a sharp interface between β' and β_t'' was captured in Fig. 9c enlarged

from the rectangular area in Fig. 9b, confirming the in-situ $\beta' \rightarrow \beta_t''$ transformation in the ternary Mg-11Y-1Al alloy. More importantly, the selected area enlarged in the bottom left corner in Fig. 9c shows that the β' phase is in the transition process, where the diffusion trace of Y atom columns can be clearly captured. Obviously, the projections of β' and β_t'' phases are different when the incident beam is parallel to $\left[11\overline{2}0\right]_\alpha$ axis, where the β_t'' phase exhibits a much higher Y concentration than that of the β' phase (Fig.9d and f). However, it shares an identical Y concentration with the β'' phase when viewing along $[0001]_\alpha$ axis (Fig. 7e and 9c). It is worth mentioning that the 18R-LPSO phase can inhibit the coarsening of precipitates (Fig. 9d) and vice versa (Fig. 9f), which will benefit for the performance of Mg-Y based alloys during long-time exposure at elevated temperatures. Fig. 10 illustrates unit cells of the β', β_t'' and β'' phases, showing the same periodicity of the β_t'' and β' phases in three primitive directions (*cbco*, $a = 0.64$ nm, $b = 2.24$ nm, $c = 0.52$ nm) and the same composition of the β_t'' and β'' phases (Mg$_3$Y).
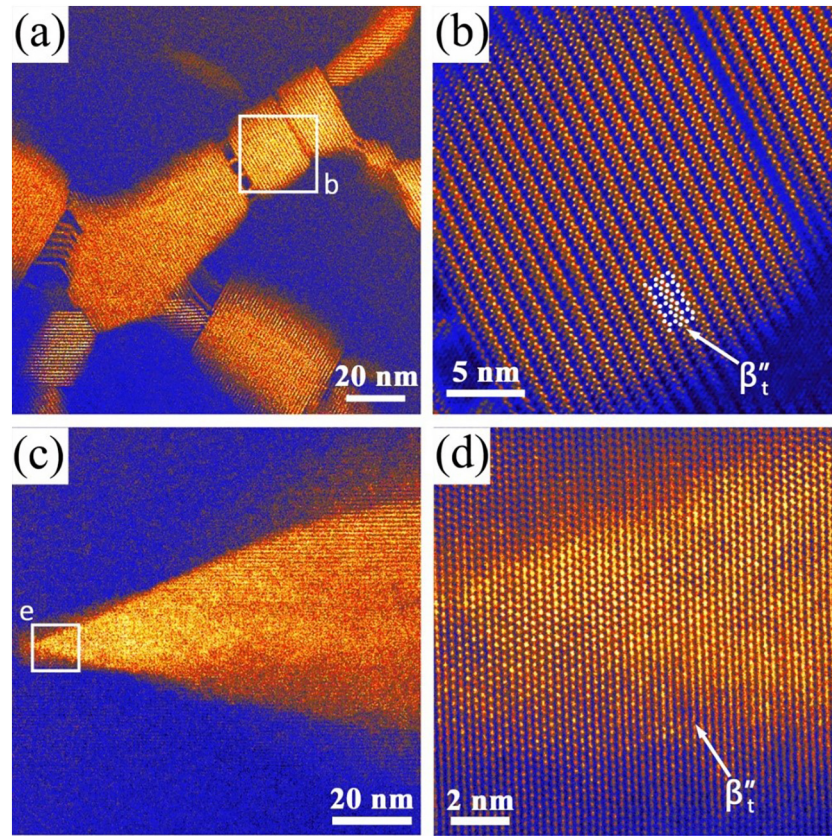
Fig. 8. HAADF-STEM images of the Mg-11Y alloys aged for 2400 h, with the electron beam parallel to (a-b) $[0001]_\alpha$ and (c-d) $[11\bar{2}0]_\alpha$, respectively.

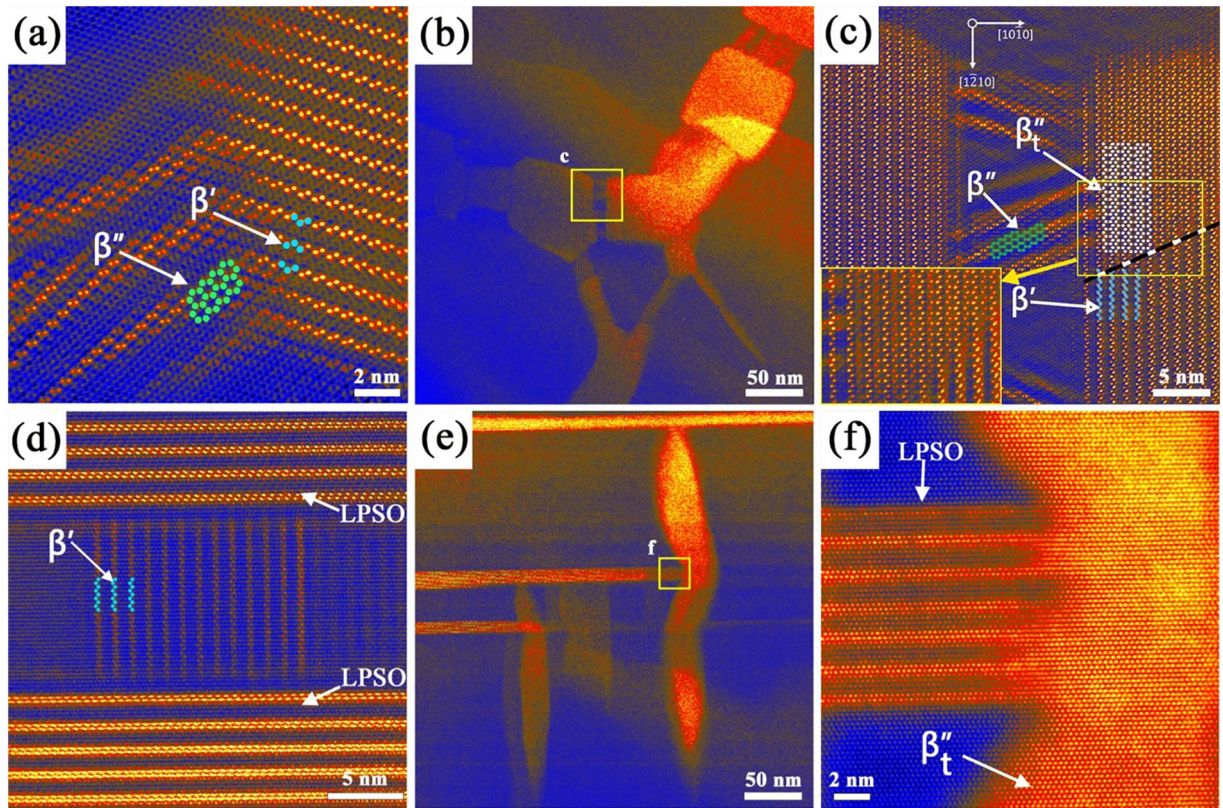Fig. 9. HAADF-STEM images of the Mg-11Y-1Al alloys (a) aged for 240 h with the electron beam parallel to $[0001]_\alpha$ and (b-f) aged for 2400 h, with the electron beam parallel to (b-c) $[0001]_\alpha$ and (d-f) $[11\bar{2}0]_\alpha$, respectively. (d) and (e) are enlarged from areas "1" and "2" in Fig. 3c, respectively, and (f) is an enlargement of selected area in (e). The difference between β', β'' and β_t'' can be well distinguished from these images.

Fig. 10. Crystal structures of (a) β'; (b) β_t''; (c) β''.
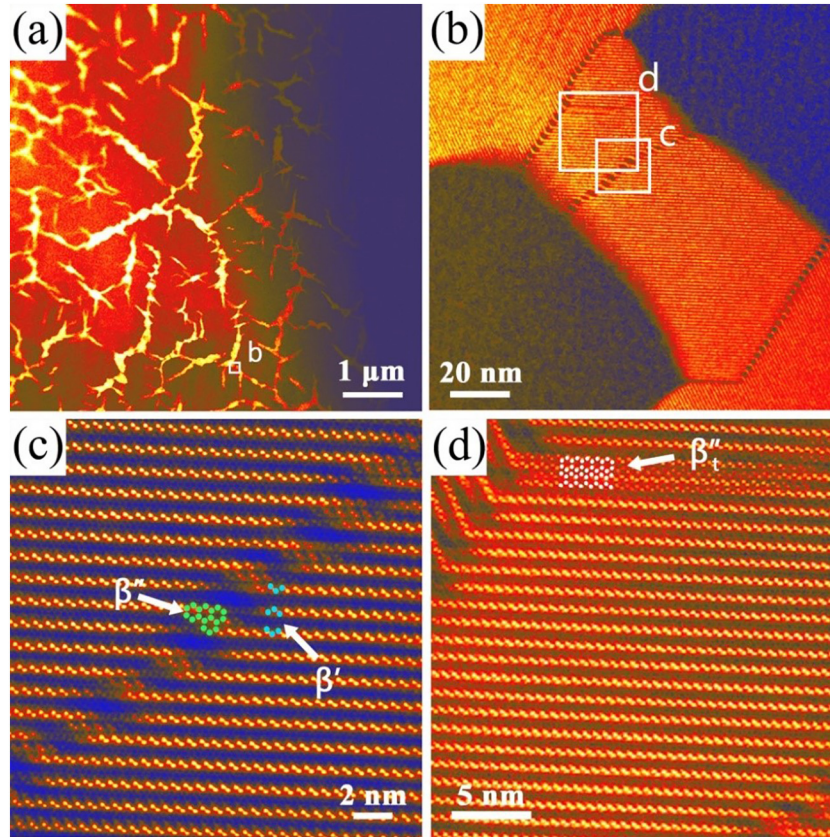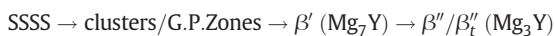

Fig. 11. HAADF-STEM images of the 550 °C-homogenized Mg-11Y-1Al alloy aged for 1200 h, with the incident beam parallel to the $[0001]_\alpha$ axis: (a) an overview of precipitate distribution; (b) an enlargement region of (a); (c) and (d) are corresponding enlargements in (b), showing the co-existence of the β', β'' and β_t'' phases.

Since the Y concentration within the matrix of 550 °C-homogenized Mg-11Y-1Al alloy is higher than that of 520 °C-homogenized Mg-11Y-1Al alloy, the in-situ phase transformation from β' to β_t'' is found clearly in the 550 °C-homogenized Mg-11Y-1Al alloy aged for 1200 h (as shown in Fig. 11), which is a bit "earlier" than that in the 520 °C-homogenized Mg-11Y-1Al alloy aged for 2400 h (Fig. 9c). But such a phenomenon appeared in the Mg-11Y alloy only consumed 480 h during ageing at 225 °C (Fig. 7d). Therefore, it is concluded that the increase of Y concentration within the matrix accelerates the formation of such a unique β_t'' phase in Mg-Y based alloys during isothermal ageing.

4. Discussion

Based on the experimental observation, the ageing sequence of Mg-Y based alloys at 225 °C should be:

$$SSSS \rightarrow clusters/G.P.Zones \rightarrow \beta' \ (Mg_7Y) \rightarrow \beta''/\beta_t'' \ (Mg_3Y)$$

In order to rationalize precipitation behavior of the Mg-Y based alloys, we characterize crystal structure of the novel β_t'' phase and calculate the formation energies of related precipitate phases hereinafter.

4.1. Crystal structure of the β_t'' phase

According to the crystallographic features aforementioned in experimental results, we proposed a *cbco* crystal structure for the β_t'' phase (Fig. 10b), which has lattice parameters of $a = 0.64$ nm, $b = 2.24$ nm, $c = 0.52$ nm and chemical composition of Mg_3Y. We further examined the *cbco* crystal structure of β_t'' phase by the HAADF-STEM simulation and compared the result with that of the β' phase. As illustrated in Fig. 12, the simulated HAADF-STEM images of the β_t'' and β' phases viewing along $[0001]_\alpha$ and $[11\bar{2}0]$ axes are all well matched with the experimental images in Figs. 8b and d. The simulated electron diffraction patterns of the β_t'' and β' phases are also attached at the top right corners in the corresponding simulated HAADF-STEM images. If we overlap the simulated electron diffraction patterns of β_t'' with β' viewing along $[0001]_\alpha$ and $[11\bar{2}0]$ axes (as shown in Fig. 12e and f), respectively, we will find out that the characteristic diffraction spots of β_t'' phase are all covered by those of the β' phase. Considering the β_t'' phase is in-situ transformed from the β' phase and can co-exist with the β' phase during long-time exposure at elevated temperatures, it is hardly distinguished β_t'' from β' in experiment only by SAED patterns.
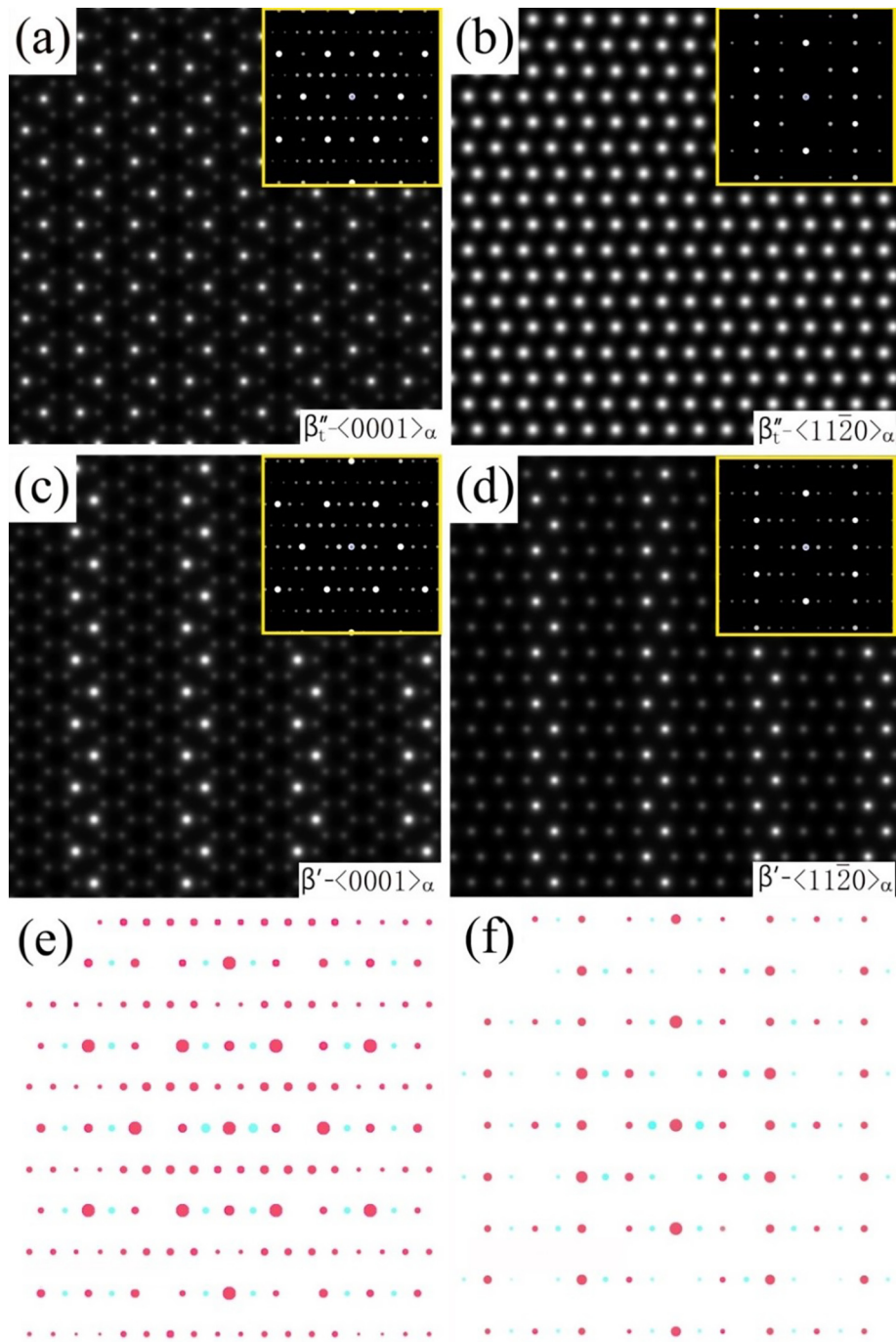
Fig. 12. Simulated HAADF-STEM images and corresponding simulated SAED patterns of the β_t'' phase with the electron beam parallel to (a) $[0001]_\alpha$ and (b) $\left[11\bar{2}0\right]_\alpha$, and compare with these of the β' phase with the electron beam parallel to (c) $[0001]_\alpha$ and (d) $\left[11\bar{2}0\right]_\alpha$. The overlapped simulated SAED patterns of the β' and β_t'' phases are enlarged in (e) $[0001]_\alpha$ and (f) viewing from $\left[11\bar{2}0\right]_\alpha$ axes, respectively. The spots in red represent the patterns for the β_t'' phase, which are totally covered by those for the β' phase regardless of the intensity difference.

Table 2
Formation energies of precipitates and comparative structures in Mg-Y system.

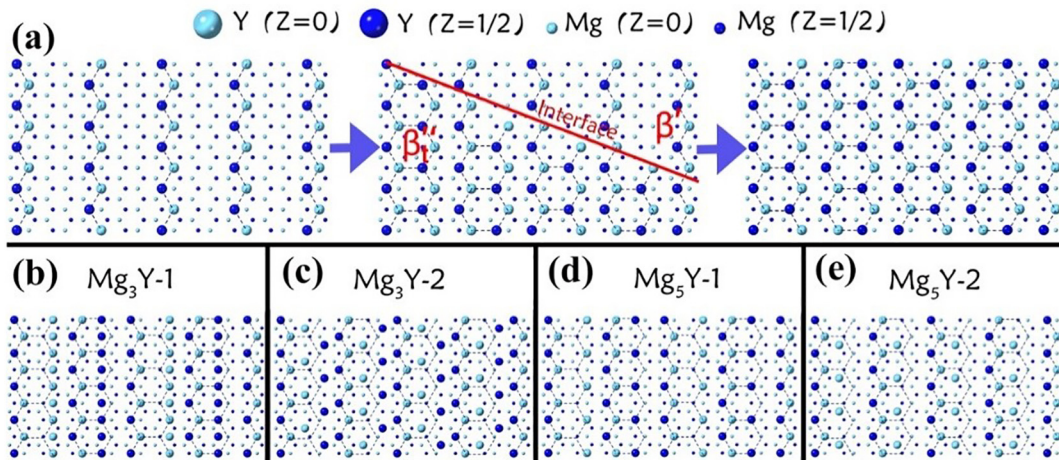| Structure	β	β'	β''	β_t''	Mg$_3$Y-1	Mg$_3$Y-2	Mg$_5$Y-1	Mg$_5$Y-2
Energy (eV/atom)	−0.08255	−0.07961	−0.10764	−0.10523	−0.05912	−0.06792	−0.05475	−0.05609

Fig. 13. (a) a schematic diagram showing the in-situ $\beta' \rightarrow \beta_t''$ phase transformation process; (b)-(e) four representative structures proposed for comparing the formation energies with that of β_t'' phase, where the compositions are Mg₃Y and Mg₅Y in (b)-(c) and (d)-(e), respectively.
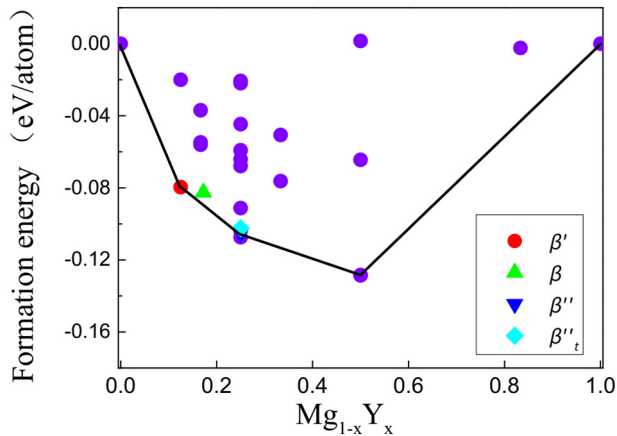

Fig. 14. Convex hull of formation energies of structures in binary Mg-Y system. The green, red, blue and teal symbols represent β, β', β'' and β_t'' phases, respectively, and the purple symbols are many representative ordering structures above the convex hull (i.e., thermodynamically unstable).

And this may be a key reason why the β_t'' phase had been ignored in the previous studies.

4.2. Formation energies of precipitates in Mg-Y based alloys

Using DFT calculations, we calculate the formation energies of these precipitates and list the results in Table 2. It is noted that the β'' and β_t'' phases not only share the same chemical composition, but also exhibit much lower formation energies than other precipitates. As clearly shown in Fig. 9c, an interface was formed when the β' phase was in-situ transformed into β_t'' phase. Hence, a schematic diagram is proposed in Fig. 13a to understand the transformation process. The Y atoms tend to gradually diffuse to the positions with relative lower energies during isothermal ageing, and the interface between β' and β_t'' would exist till the transformation process is complete. Several possible structures with a composition of Mg₃Y are also selected in order to compare their formation energies with the novel β_t'' phase by using convex hull simulation [37,38]. The result in Fig. 14 indicates that the β_t'' phase, which has a close formation energy value with the β'' phase, exhibits a much lower formation energy value than the other Mg₃Y-structures. Two representative Mg₃Y-1 and Mg₃Y-2 structures with a higher

symmetry are illustrated in Fig. 13b and 13c for comparing the distribution of Y atoms with the β_t'' phase, respectively. In addition, the Y concentration of precipitate is increased during the in-situ $\beta' \rightarrow \beta_t''$ transformation, which raises a question spontaneously that whether there is a possible metastable phase during the transformation. Since the Mg₅RE-structures have been reported in some Mg-RE systems [1], we herein propose two representative high-symmetry structures in Fig. 13d (Mg₅Y-1) and 13e (Mg₅Y-2) for comparison, and their corresponding formation energies are listed in Table 2. The Mg₅Y-structures show higher formation energies than that of any precipitate observed in Mg-Y based alloys, indicating it is impossible to form a Mg₅Y-structure during ageing in the in-situ $\beta' \rightarrow \beta_t''$ transformation.

The convex hull connecting the most stable phases with the same compositions is shown as black solid line in Fig. 14. Although formation energies of the β'' (−0.10764 eV/atom) and β_t'' (−0.10523 eV/atom) phases do not lie exactly on the convex hull, they share a very close formation energy with the Mg₃Y superstructure on the convex-hull (−0.10785 eV/atom). Although the DFT calculation is conducted at 0 K, the β'' and β_t'' phases formed during ageing at elevated temperature are still reasonable. With respect to the β phase (Mg₂₄Y₅) reported in the literature [1,13], its formation energy is obviously above the convex hull, suggesting that it is not energetically favorable in this case. With increasing temperatures, vibrational entropy becomes significant, and the β phase is predicted to be stable above 520 K [14]. This well explains why the β phase is not observed during ageing at 225 °C in our paper. Moreover, such a β phase has not been observed experimentally during ageing at temperatures lower than 300 °C [13,15].

As aforementioned, 1 wt. pct Al addition does not alter the ageing sequence of Mg-Y based alloys. In order to investigate the effect of Al addition on the precipitation behavior during isothermal ageing in Mg-Y based alloys thermodynamically, the formation energies of four precipitates (β, β', β'' and β_t'') with different Al substitutions were calculated, as shown in Fig. 15. And the lowest formation energy for each single Al substitution is listed in Table 3. Specifically, the values listed in Table 3 refer to those of Al₁ (substitution for Mg) and Al₃ (substitution for Y) for β, Al₈ (substitution for Mg) and Al₃ (substitution for Y) for β', Al₂ (substitution for Mg) and Al₄ (substitution for Y) for β'', Al₆ (substitution for Mg) and Al₁₁ (substitution for Y) for β_t'', respectively. The results show that the Al atom prefers to substitute the Mg atom rather than the Y atom in the four phases, and the β'' and β_t'' always exhibit a lower formation energies after the substitution. In addition, these possible substitutions would not change the precipitate structures, indicating that the Al addition had little impact on the precipitation behavior of Mg-Y based alloys.
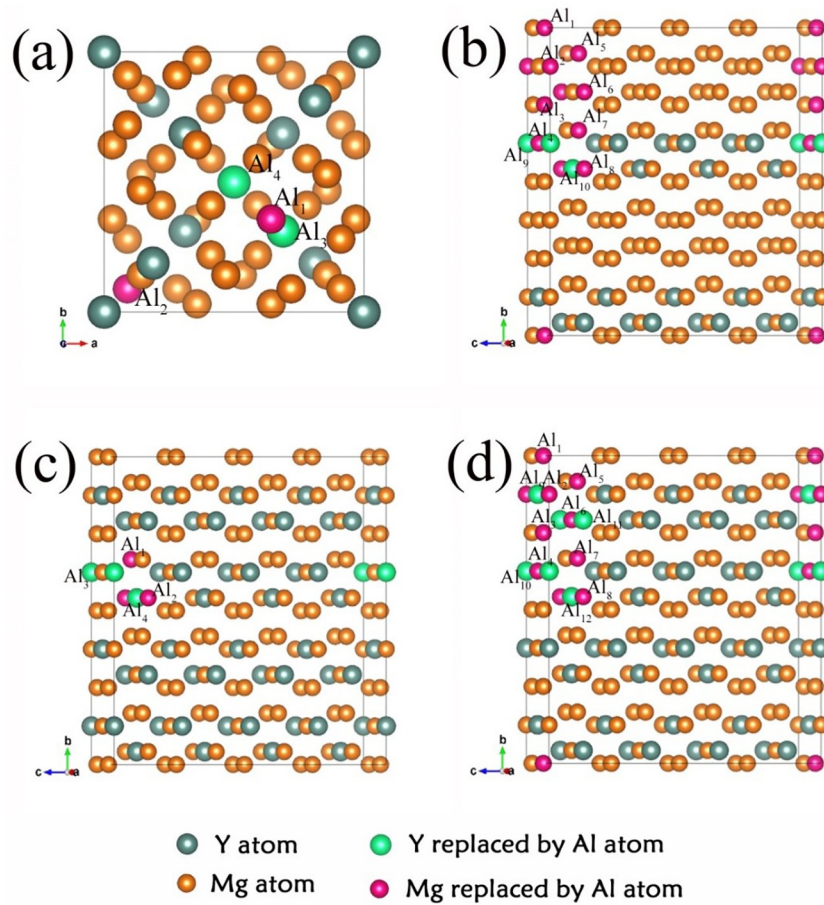
Fig. 15. Models of possible Al substitutions for Mg or Y characteristic sites in (a) β; (b) β'; (c) β''; (d) β_t''. The balls colored with yellow, teal, pink and green represent atoms of Mg, Y, Al substitution for Mg and Al substitution for Y, respectively. The Mg and Y atoms in these structures are considered to be replaced for only once at a time. The possible positions for the substitutions in four structures are marked as "A$_1$" to "Al$_{12}$" in the corresponding figures.

Table 3
Formation energies of precipitates in the Mg-Y and Mg-Y-Al alloys.

	β	β'	β''	β_t''
Binary(eV/atom)	−0.08255	−0.07961	−0.10764	−0.10523
Al replace Mg atom(eV/atom)	−0.08526	−0.80217	−0.10975	−0.10885
Al replace Y atom(eV/atom)	−0.08125	−0.07812	−0.10596	−0.10398

5. Conclusions

The aim of this work is to understand the precipitation behavior in Mg-Y based alloys during isothermal ageing. Via combining atomic resolution HAADF-STEM characterization with DFT calculations, an undiscovered precipitation behavior in Mg-Y based alloys has been unveiled, and the main conclusions are summarized as follows:

(1) The precipitation sequence of Mg-Y based alloys during ageing at 225 °C has been proved to be SSSS → clusters/G.P. Zones →β' (Mg$_7$Y) → β''/β_t'' (Mg$_3$Y). A new phase named β_t'', which shares the same chemical composition with the β'' phase, forms through in-situ transformation from the β' phase. The DFT calculations rationalize the precipitation behavior, especially the formation of β_t'' phase.

(2) Although the micro-alloying Al does not alter the precipitation sequence of Mg-Y based alloys, the density and distribution of precipitates can be controlled via tuning the volume fractions of LPSO phase.

(3) The novel β_t'' phase, with the co-existence of β', β'' and LPSO phases, exhibits a remarkable thermal stability after ageing at 225 °C for 2400 h. More importantly, the LPSO phase can strongly inhibit the coarsening of precipitates during long-time exposure at elevated temperature, and vice versa, which provides a much more flexible strategy on manipulating precipitation strengthening in Mg-Y based alloys.

Data availability

The related data of this study are available from the corresponding authors upon reasonable request.

Credit author statement

Q.C. Zhu. and Y.X. Li. conceived the idea, carried out the structural analyses using HAADF-STEM and wrote the manuscript. Q.C. Zhu., H. Zhang. and Y.X. Liu. prepared the alloys. Q.C. Zhu., Z.G. Ding., T. Xie. and M.X. Wang were responsible for the DFT calculation. All authors contributed to the interpretation of the results and to the writing of the paper.

Declaration of Competing Interest

The authors declare that they have no known competing financial interests or personal relationships that could have appeared to influence the work reported in this paper.

Acknowledgement

References

[1] J.-F. Nie, Precipitation and hardening in magnesium alloys, Metall. Mater. Trans. A 43 (11) (2012) 3891–3939.

[2] J. Song, J. She, D. Chen, F. Pan, Latest research advances on magnesium and magnesium alloys worldwide, J. Mag. and Alloys 8 (1) (2020) 1–41.

[3] J. Zhang, S. Liu, R. Wu, L. Hou, M. Zhang, Recent developments in high-strength Mg-RE-based alloys: focusing on Mg-Gd and Mg-Y systems, J. Mag. and Alloys 6 (3) (2018) 277–291.

[4] R. Alizadeh, J. Llorca, Interactions between basal dislocations and $\beta 1'$ precipitates in Mg–4Zn alloy: mechanisms and strengthening, Acta Mater. 186 (2020) 475–486.

[5] C.Y. Wang, C.M. Cepeda-Jiménez, M.T. Pérez-Prado, Dislocation-particle interactions in magnesium alloys, Acta Mater. 194 (2020) 190–206.

[6] L. Wang, J. Sabisch, E.T. Lilleodden, Kink formation and concomitant twin nucleation in Mg–Y, Scr. Mater. 111 (2016) 68–71.

[7] K.H.Y. Kawamura, A. Inoue, T. Masumoto, Rapidly solidified powder metallurgy Mg97Zn1Y2 alloys with excellent tensile yield strength above 600 MPa, Mater. Trans. 42 (7) (2001).

[8] L.L. Rokhlin, Magnesium alloys containing rare earth metals: structure and properties, CRC2003.

[9] S. Sandlöbes, M. Friák, J. Neugebauer, D. Raabe, Basal and non-basal dislocation slip in Mg–Y, Mater. Sci. Eng. A 576 (2013) 61–68.

[10] A. Inoue, Y. Kawamura, M. Matsushita, K. Hayashi, J. Koike, Novel hexagonal structure and ultrahigh strength of magnesium solid solution in the Mg–Zn–Y system, J. Mater. Res. 16 (07) (2001) 1894–1900.

[11] Y.M. Zhu, A.J. Morton, J.F. Nie, The 18R and 14H long-period stacking ordered structures in Mg–Y–Zn alloys, Acta Mater. 58 (8) (2010) 2936–2947.

[12] M. Nishijima, K. Yubuta, K. Hiraga, Characterization of β' precipitate phase in Mg-2 at% Y alloy aged to peak hardness condition by high-angle annular detector dark-field scanning transmission Electron microscopy(HAADF-STEM), Mater. Trans. 48 (1) (2007) 84–87.

[13] M.X. Zhang, P.M. Kelly, Morphology and crystallography of $Mg_{24}Y_5$ precipitate in Mg–Y alloy, Scr. Mater. 48 (4) (2003) 379–384.

[14] E.L.S. Solomon, A.R. Natarajan, A.M. Roy, V. Sundararaghavan, A. Van der Ven, E.A. Marquis, Stability and strain-driven evolution of β' precipitate in Mg–Y alloys, Acta Mater. 166 (2019) 148–157.

[15] Sato Tatsuo, Takahashi Isao, Tezuka Hiroyasu, Kamio Akihiko, Precipitation structures of Mg-Y alloys, J Japan Institute of Light Metals 42 (1992) 804–809.

[16] D. Wang, M. Amsler, V.I. Hegde, J.E. Saal, A. Issa, B.-C. Zhou, X. Zeng, C. Wolverton, Crystal structure, energetics, and phase stability of strengthening precipitates in Mg alloys: a first-principles study, Acta Mater. 158 (2018) 65–78.

[17] K. Saito, A. Yasuhara, M. Nishijima, K. Hiraga, Structural changes of precipitates by aging of an Mg-4 at%Dy solid solution studied by atomic-scaled transmission Electron microscopy, Mater. Trans. 52 (5) (2011) 1009–1015.

[18] K. Saito, K. Hiraga, The Structures of Precipitates in an Mg-0.5 at%Nd Age-Hardened Alloy Studied by HAADF-STEM Technique, Mater. Trans. 52 (10) (2011) 1860–1867.

[19] M. Nishijima, K. Hiraga, M. Yamasaki, Y. Kawamura, Characterization of precipitates in Mg-Sm alloy aged at 200°C, studied by high-resolution transmission Electron microscopy and high-angle annular detector dark-field scanning transmission Electron microscopy, Mater. Trans. 50 (7) (2009) 1747–1752.

[20] M. Nishijima, K. Hiraga, Structural changes of precipitates in an Mg-5 at%Gd alloy studied by transmission Electron microscopy, Mater. Trans. 48 (1) (2007) 10–15.

[21] J.F. Nie, N.C. Wilson, Y.M. Zhu, Z. Xu, Solute clusters and GP zones in binary Mg–RE alloys, Acta Mater. 106 (2016) 260–271.

[22] T.J. Pike, B. Noble, The formation and structure of precipitates in a dilute magnesium-neodymium alloy, J. Less Common Metals 30 (1) (1973) 63–74.

[23] W. Lefebvre, V. Kopp, C. Pareige, Nano-precipitates made of atomic pillars revealed by single atom detection in a Mg-Nd alloy, Appl. Phys. Lett. 100 (14) (2012).

[24] Y. Matsuoka, K. Matsuda, K. Watanabe, J. Nakamura, W. Lefebvre, D. Nakagawa, S. Saikawa, S. Ikeno, Precipitation sequence in the Mg-Gd-Y system investigated by HRTEM and HAADF-STEM, Mater. Trans. 55 (7) (2014) 1051–1057.

[25] H. Zhang, C.Q. Liu, Y.M. Zhu, H.W. Chen, L. Bourgeois, J.F. Nie, Revisiting building block ordering of long-period stacking ordered structures in Mg–Y–Al alloys, Acta Mater. 152 (2018) 96–106.

[26] Y. Li, C. Yang, X. Zeng, P. Jin, D. Qiu, W. Ding, Microstructure evolution and mechanical properties of magnesium alloys containing long period stacking ordered phase, Mater. Charact. 141 (2018) 286–295.

[27] Z.Z. Peng, X.H. Shao, X.W. Guo, J. Wang, Y.J. Wang, X.L. Ma, Atomic-scale insight into structure and Interface of Al_2 Y phase in an Mg-Al-Y alloy, Adv. Eng. Mater. 20 (4) (2018).

[28] G. Kresse, Ab initio molecular dynamics for liquid metals, J. Non-Cryst. Solids 192-193 (1995) 222–229.

[29] G. Kresse, J. Furthmüller, Efficiency of ab-initio total energy calculations for metals and semiconductors using a plane-wave basis set, Comput. Mater. Sci. 6 (1) (1996) 15–50.

[30] G. Kresse, J. Furthmuller, Efficient iterative schemes for ab initio total-energy calculations using a plane-wave basis set, physical review, B, Condensed matter 54 (16) (1996) 11169–11186.

[31] P.E. Blochl, Projector augmented-wave method, physical review, B, Condensed matter 50 (24) (1994) 17953–17979.

[32] G. Kresse, J. Hafner, Norm-conserving and ultrasoft pseudopotentials for first-row and transition elements, J. Phys. Condens. Matter 6 (1999) 8245.

[33] J. Perdew, K. Burke, M. Ernzerhof, Generalized gradient approximation made simple, Phys. Rev. Lett. 77 (1996) 3865–3868.

[34] E. Cockayne, A. van de Walle, Building Effective Models from Sparse but Precise Data: Application to an Alloy Cluster Expansion Model, Physical Review B 81, 2010.

[35] A. van de Walle, G. Ceder, Automating first-principles phase diagram calculations, J. Phase Equilibria 23 (4) (2002) 348.

[36] A. van de Walle, R. Sun, Q.-J. Hong, S. Kadkhodaei, Software tools for high-throughput CALPHAD from first-principles data, Calphad 58 (2017) 70–81.

[37] A.R. Natarajan, A. Van der Ven, A unified description of ordering in HCP Mg-RE alloys, Acta Mater. 124 (2017) 620–632.

[38] L. Tang, W. Liu, Z. Ding, D. Zhang, Y. Zhao, E.J. Lavernia, Y. Zhu, Alloying Mg with Gd and Y: increasing both plasticity and strength, Comput. Mater. Sci. 115 (2016) 85–91.